Reduction of CO_2 to Methanol: photocatalytic and electrocatalytic process on photocatalyst

Zambaga Otgonbayar[1], Chang Sung Lim [1], Yonrapach Areerob [2], Tongso Park [3], Won-Chun Oh [1*]

[1] Department of Advanced Materials Science & Engineering, Hanseo University,
Chungnam 356-706, South Korea
[2] Faculty of Engineering, King Mongkul's Institute of Technology Ladkrabang, Bangkok 10520, Thailand
[3] Department of Infra-system, Hanseo University, Seosan, Chungnam Korea, 31

Abstract: Increasing CO_2 concentration in the atmosphere is believed to have a profound impact on the global climate. To reverse the impact would necessitate not only curbing the reliance on fossil fuels but also developing effective strategies capture and utilize CO_2 from the atmosphere. Among several available strategies, CO_2 reduction via the electrochemical or photochemical approach is particularly attractive since the required energy input can be potentially supplied from renewable sources such as solar energy. The electrochemical reduction of carbon dioxide is the conversion of carbon dioxide (CO_2) to more reduced chemical species using electrical energy. Photocatalytic carbon dioxide (CO_2) reduction to obtain hydrocarbon solar fuels is one of the promising strategies to solve energy crisis and complement carbon cycle. The reduction processes mainly based on the catalyst material, and the design and structure of the catalyst strongly affect to how the carbon dioxide converts into hydrocarbon fuels. This review paper mainly presents the influence of various factors on the catalytic reduction performance, the type of catalyst and the reaction mechanism.

Keywords: reduction of CO_2, reduction method, catalyst, structure, methanol, 2D-graphene.

1. Introduction

The chemical industry of today is largely dependent on fossil fuels. Oil, gas and coal are used both as feedstock and as fuel to power the conversion and separation processes. Consequently, the industry is a major emitter of CO_2 and other greenhouse gases. The increasing greenhouse gas CO_2 concentration level in atmosphere raises serious concerns on fossil fuel-based energy supply. Renewable energy sources, such as solar, wind, hydro, and waves, are being considered as potential alternatives because they are more sustainable and carbon-neutral. Since late 19th century (in Figure 1), CO_2 concentration in the atmosphere has increased from 280 to 400 ppm [1-7].
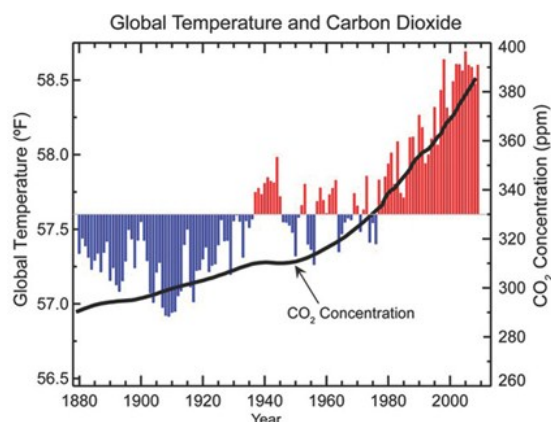
Figure 1. Atmospheric CO$_2$ concentration and corresponding global average temperature since the late 19th century. Red bars indicate temperatures above and blue bars indicate temperatures below the 1901–2000 average temperature [5].

In nature, the photosynthesis of green plants plays an indispensable role in maintaining the carbon/oxygen cycle which is vital for the maintenance of life on earth. It is consisted of two sequential steps known as the light and dark reactions (in Figure 2a). In the light reaction, chlorophyll adsorbs sunlight, converts it to the chemical energy stored in adenosine triphosphate (ATP), and meanwhile oxidizes water to O$_2$. In the dark reaction, CO$_2$ is fixed and reduced stepwise to form carbohydrates using energy stored in ATP. The natural photosynthesis essentially provides the energy needed for most lives on this planet and is the basis for the survival of mankind [8-16]. For more than three decades, researchers have been ambitiously attempting to mimic what Nature does and pursuing artificial photosynthesis that aims at the spontaneous transformation of atmospheric CO$_2$ and water to chemical fuels using sunlight as the sole energy input. Although still at very low efficiency currently, artificial photosynthesis is believed to have the great potential to make a substantial contribution to our future energy supply. It is now generally approached from two directions. As schematically illustrated in Figure 2b, the first route uses photovoltaic (PV) cells to generate a sufficient photovoltage which is then supplied to the cathode for the CO$_2$ reduction and the anode for the water oxidation. Proper electrocatalysts are employed on the two electrodes so as to expedite the reaction rate and improve the reaction selectivity. The advantage of this route is the flexibility in the design of PV and electrocatalyst pairs. Components can be individually optimized and then combined together to enable the best overall performance. The second route is the direct photocatalytic approach where light-absorbing semiconductor particles (photocatalysts) decorated with suitable electrocatalysts (commonly referred as cocatalysts in photocatalysis) are dispersed in aqueous solution and achieve light harvesting, charge separation, and interfacial charge transfer to drive corresponding reactions all within particles (in Figure 2c). The merit of the second route is its wireless configuration that renders the device design much more straightforward and compact [17-20]. Their future success strongly relies on the development of high-performance CO$_2$ reduction electrocatalysts or photocatalysts.
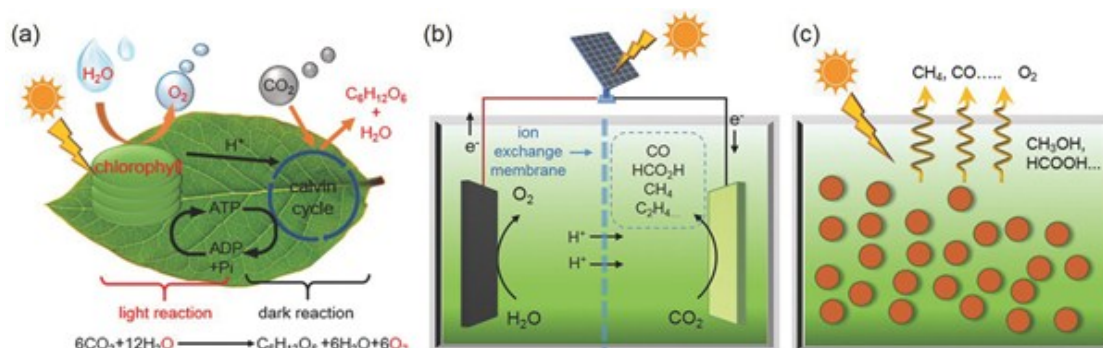
Figure 2. Analogy among a) natural photosynthesis, b) electrochemical synthesis on electrocatalysts powered by a photovoltaic cell, and c) photochemical synthesis on powdery photocatalysts [20].

CO$_2$ is one of the most thermodynamically stable molecules due to the strong C-O double bond with bonding energy of 750 kJ mol^{-1}—considerably larger than that of C-C (336 kJ mol^{-1}), C-O (327 kJ mol^{-1}), or C-H bond (411 kJ mol^{-1}). CO$_2$ reduction via either the electrocatalytic or the photocatalytic approach is a thermodynamically uphill reaction and demands significant energy input to break the C-O bond. To make it even more complicated, CO$_2$ reduction may proceed via several different reaction pathways with the transfer of 2, 4, 6, 8, 12 or even more electrons and yielding diverse reduction products including carbon monoxide (CO), formic acid (HCOOH), methane (CH$_4$), ethylene (C$_2$H$_4$), and many others depending on the nature of the electrocatalysts or photocatalysts as well as the actual experimental conditions [21].

2. Reduction method

Three main approaches suggested to reduce the amounts of CO$_2$ in the atmosphere which includes 1. Direct lowering of CO$_2$ emissions, 2. CO$_2$ capture and storage (CCS), 3. CO$_2$ utilization and transformation. Typically, several technologies have been utilized for the CO2 transformation to hydrocarbon fuels, including thermodynamical, biological, photoelectrocatalytic, electrocatalytic and photocatalytic reduction reactions. Among them, electrocatalytic and photocatalytic methods are widely studied in the CO$_2$ reduction study. Both methods have their own specific advantages [22].

Photochemical reduction of CO$_2$ with H$_2$O using solar light and semiconductor photocatalysts mimicking the natural photosynthesis process in plants can realize the potential scalable production of so-called solar fuels (CH$_3$OH, C$_2$H$_5$OH, and hydrocarbons) at a satisfactory purity (in Figure 3). There are several methods used for the reduction of CO$_2$; among them, photocatalytic and electrochemical reduction methods are widely used in research investigating CO$_2$ conversion [23]. The photocatalytic method has the advantage of being a conventional low-energy technology, and it can efficiently convert and store solar energy into chemical energy while allowing carbon to be recycled. The whole photocatalytic CO$_2$ reduction process consists of five stages: light absorption, charge separation, adsorption of CO$_2$ onto the surface of photocatalyst, surface redox reaction, and product desorption.
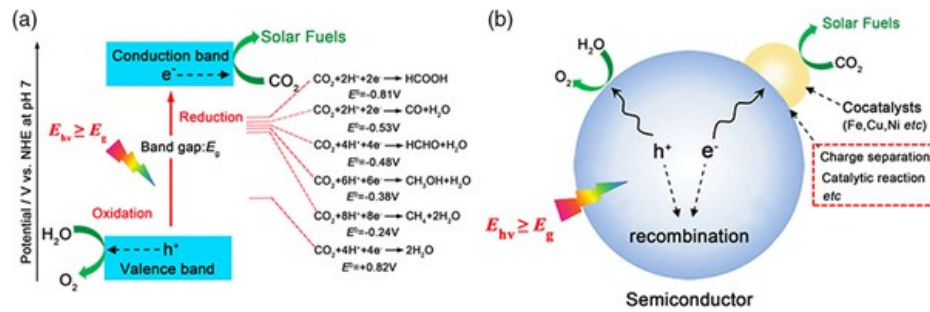
Figure 3. a) Schematic energy diagram for CO_2 reduction and H_2O oxidation on a semiconductor. b) Schematic of the overall photocatalytic reaction process, illustrating factors that may impact photocatalytic performance [21]

The reduction potential for the various products of CO_2 reduction at pH 7 is presented in Table 1. On the one hand, single-electron CO_2 reduction reaction requires a highly negative potential of 1.9 eV, which makes the one-electron reduction process very unfavorable. On the other hand, the proton assisted multi-electron CO_2 reduction reaction requires comparatively low redox potential (Table 1) and are more favorable. Photocatalysts can facilitate these reduction processes with lower potential. For this purpose, an ideal photocatalyst generally requires two characteristics: (i) the redox potential of the photo-excited VB hole must be sufficiently positive so that the hole can act as an electron acceptor; and (ii) the redox potentials of the photo-excited CB electron must be more negative than that of the CO_2/reduced-product redox couple [22].

Reactions	E^0/eV
$CO_2 + e^- \rightarrow CO_2$	≥ -1.9
$CO_2 + 2e^- + 2H^+ \rightarrow HCOOH$	-0.61
$CO_2 + 2e^- + 2H^+ \rightarrow CO + H_2O$	-0.53
$CO_2 + 4e^- + 4H^+ \rightarrow HCHO + H_2O$	-0.48
$CO_2 + 6e^- + 6H^+ \rightarrow CH_3OH + H_2O$	-0.38
$CO_2 + 8e^- + 8H^+ \rightarrow CH_4 + 2H_2O$	-0.24

The photocatalytic CO_2 reduction efficiency is generally measured by the yield of the product. Here, the general unit for R is mol·h^{-1}·g^{-1} of catalyst and for the product either in molar units (ìmol) or in concentration units (ppm).

$$R = n(Product) \ / \ Time \times m(Catalysts) \qquad (1)$$

In the catalyst-based measurements, the efficiency of the photocatalyst usually depends on the amount of photocatalyst, the intensity of the light, lighting area, etc., so under the irradiation of light, the amount of product formed by per gram of photocatalyst within a certain time period can be measured by its apparent quantum yield. It is calculated by using the amount of product and the incident photon number as shown in the following equations [23, 24]. When the photocatalytic reduction reaction gives

complex products, then the number of reacted electrons in the equation denotes the sum of the reacted electron to form each product [25, 26]. Thus, in light-based measurements, the quantum yield of CO$_2$ photo-reduction into different products can be calculated using following equations:

$$Overall\ quantum\ yield(\%) = \frac{Number\ of\ reacted\ electrons}{Number\ of\ absorbed\ photons} \times 100\% \qquad (2)$$

$$Apparent\ quantum\ yield(QY, \%) = \frac{Number\ of\ reacted\ electrons}{Number\ of\ incident\ photons} \times 100\% \qquad (3)$$

$$(Apparent)\ quantum\ yield\ of\ CO(\%) = \frac{2 \times Number\ of\ CO\ molecules}{Number\ of\ incident\ photons} \times 100\% \qquad (4)$$

$$(Apparent)\ quantum\ yield\ of\ HCOOH(\%) = \frac{2 \times Number\ of\ HCOOH\ molecules}{Number\ of\ incident\ photons} \times 100\% \qquad (5)$$

$$(Apparent)\ quantum\ yield\ of\ HCHO(\%) = \frac{4 \times Number\ of\ HCHO\ molecules}{Number\ of\ incident\ photons} \times 100\% \qquad (6)$$

$$(Apparent)\ quantum\ yield\ of\ CH3OH(\%) = \frac{6 \times Number\ of\ CH3OH\ molecules}{Number\ of\ incident\ photons} \times 100\% \qquad (7)$$

$$(Apparent)\ quantum\ yield\ of\ CH4(\%) = \frac{8 \times Number\ of\ CH4\ molecules}{Number\ of\ incident\ photons} \times 100\% \qquad (8)$$

Moreover, the electrochemical CO$_2$ reduction method has been studied in a latitudinal manner, attracting attention for its operational parameters, faradaic efficiency, and simplicity. The term of "electro-fuel" refers to liquid fuels that are produced by electrochemical means. The overall scheme is outlined in Figure 4, where an electrochemical reactor, such as an electrolyzer, is powered by electricity generated from renewable sources to drive an energy uphill process that converts CO$_2$ and H$_2$O into electro-fuels [27]. The resulting electro-fuels can be easily stored, distributed, and used to power transportation and other human activities through the existing infrastructure. CO$_2$ and H$_2$O generated during the consumption of electro-fuels are captured and fed back to the reactor to close the loop.
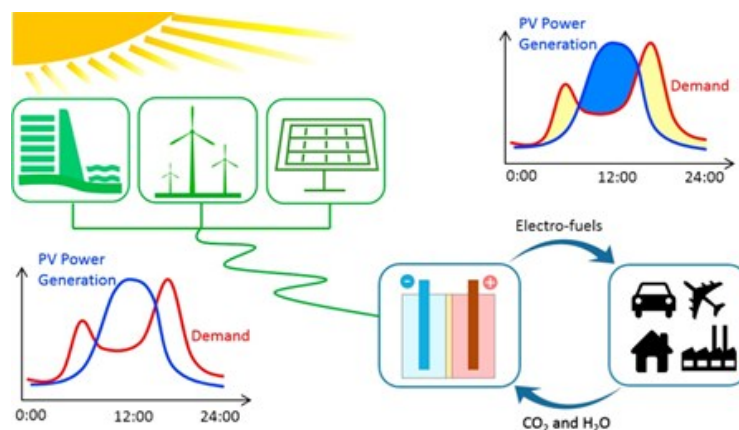

Figure 4. An overall schematic of electro-fuel enabled energy storage to migrate the mismatch between renewable energy generation (photovoltaic as an example) and energy demand.

The key step to convert CO_2 into an electro-fuel is the chemical transformation of CO_2 molecule into reduced carbon species, which is a difficult process due to the poor kinetics of CO_2 electroreduction. The electrochemical CO_2 reduction becomes more attractive because it has a few characteristic advantages compared to other approaches [28-31]. For example, the reaction can be conducted at ambient conditions with the reaction rate easily controlled by tuning the external bias (*i.e.* overpotential). The products are produced at different electrodes, enabling natural separation using individual reaction chambers, which minimizes the cost associated with post-reaction separation processes. In a typical CO_2 electrolyzer, anode and cathode are placed in two chambers separated with an ion conducting membrane. At anode, water is oxidized to molecular oxygen, whereas CO_2 is reduced to reduced carbon pieces at cathode (in Figure 5).
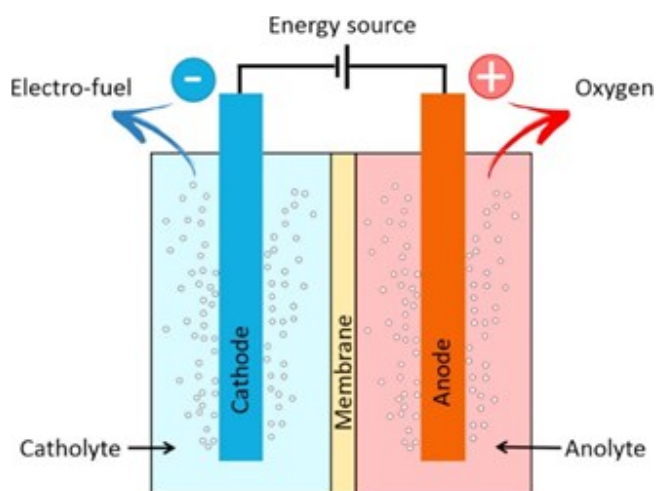

Figure 5. A typical schematic of an ion-conducting membrane based CO_2 electrolyzer [31].

3. Synthesis of photocatalyst

Several catalyst material suggested in photocatalytic and electrochemical reduction of CO_2 and several strategies developed to improve the activity of those catalyst. The first step towards enhancing the photocatalytic activity is the selection of a proper photocatalyst. It is a subject of considerable importance both for practical application of photocatalysts and understanding their mechanism. Photocatalysts could be categorized into two basic groups based on their structures: homogeneous and heterogeneous photocatalysts. Figure 6 shows the studies on photocatalytic CO_2 reduction with H_2O to obtain good efficiency and selectivity for specific products. However, this approach is still far from practical implementation. Application of photocatalysis in the environmental and energy industries on a large scale is still limited. Among several difficulties in the heterogeneous photocatalysis, the two major ones are low photocatalytic efficiency and the lack of suitable visible-light-responsive photocatalyst [32, 33]. The first one is mostly because of the recombination of photo-generated electrons and holes.
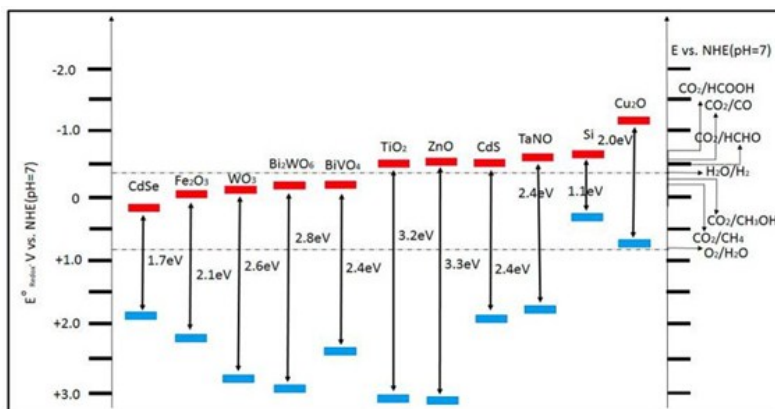
Figure 6. Schematic representation of conduction band, valence band potentials, and band gap energies of various semiconductor photocatalysts and relative redox potentials of the compounds involved in CO$_2$ reduction at pH 7 [32].

The photocatalytic CO$_2$ reduction is a very effective method considering that no additional energy is needed and no negative effect on the environment is produced. The use of cheap and abundant sunlight to transform this major greenhouse gas into other carbon containing products is also an ideal approach because of its low cost. Here, the high activation energy to break very stable CO$_2$ molecule is provided by solar energy [34]. To date, many photocatalysts, including oxides and non-oxides, e.g., TiO$_2$, ZnO, Fe$_2$O$_3$, ZrO$_2$, SnO$_2$, BiWO$_3$, Ti-MCM-41, CdS, TNTs, ZnS, GaN, and SiC, have been studied for the photocatalytic reduction of CO$_2$ with H$_2$O. A summary of different photocatalytic systems employed in this technology since 2010 are given in Table 1.

Table 1. Advances in Photocatalytic systems for CO_2 reduction with water since the year 2010.

Photocatalyst	Radiation Source	Major Products	Comments	References
0.5 wt % Cu/TiO_2-SiO_2	Xe lamp (2.4 mW cm^{-2}, 250–400 nm)	CO and CH_4	The synergistic combination of Cu deposition and high surface area of SiO_2 support enhanced CO_2 photoreduction rates.	[35]
$ZnGa_2O_4$	300 W Xe arc lamp	CH_4	Strong gas adsorption and large specific surface area of the mesoporous $ZnGa_2O_4$ photocatalyst contribute to its high photocatalytic activity for converting CO_2 into CH_4.	[36]
(RuO + Pt)-Zn_2GeO_4	300 W Xe arc lamp	CH_4	In the presence of water, ultra-long and ultrathin geometry of the Zn_2GeO_4 nano-ribbon promotes CO_2 photo-reduction, which was significantly enhanced by loading of Pt or RuO_2.	[37]
$Ag/ALa_4Ti_4O_{15}$ (A = Ca, Ba and Sr)	400 W Hg lamp	CO, HCOOH, and H_2	On the optimized $Ag/BaLa_4Ti_4O_{15}$ photocatalyst, CO was the reported as the main product. The molar ratio of O_2 production (H_2 + CO:O_2 = 2:1) demonstrated that water was consumed as a reducing reagent in the photocatalytic process.	[38]
I-TiO_2 nanoparticles	450 W Xe lamp	CO	High photocatalytic activity was observed under visible light and the efficiency of CO_2 photoreaction was much greater than undoped TiO_2 due to the extension in the absorption spectra of TiO_2 to the visible light region and facilitated charge separation.	[39]
$LiNbO_3$	Natural sunlight or Hg lamp (64.2 mW cm^{-2})	HCOOH	The MgO-doped $LiNbO_3$ showed an energy conversion efficiency rate of 0.72% which was lower than that for the gas–solid catalytic reaction of $LiNbO_3$ (2.2%).	[40]
G-$Ti_{0.91}O_2$ hollow spheres	300 W Xe arc lamp	CH_4, CO	The presence of G nanosheets compactly stacking with $Ti_{0.91}O_2$ nanosheets allows the rapid migration of photo-generated electrons from $Ti_{0.91}O_2$ nanosheets into G and improves the efficiency of the photocatalytic process.	[41]

Figure 7a shows the advantages of H_2O oxidation of a metal complex catalyst (H_2O oxidation site) with a sacrificial electron acceptor (SA). Figure 7b shows the advantages of CO_2 reduction for a metal complex catalyst (CO_2 reduction site) with a sacrificial electron donor (SD). Figure 7c shows the problems encountered when combining H_2O oxidation site and CO_2 reduction site: (I) reverse oxidation of products such as organic compounds; (II) electron transfer from H_2O oxidation site to CO_2 reduction site; (III) need to be electron storage; (IV) need to be active in H_2O; (V) easier reduction of O_2 than CO_2; and (VI) stability in H_2O. A number of challenges are encountered in constructing a homogeneous metal complex system for CO_2 reduction along with H_2O oxidation. The inefficient electron transport between reduction and oxidation catalysts is one of the major difficulties in this process. Another drawback is the short lifetimes of the one-electron-reduced species and the photo-excited state in the presence of O_2 generated by H_2O oxidation.
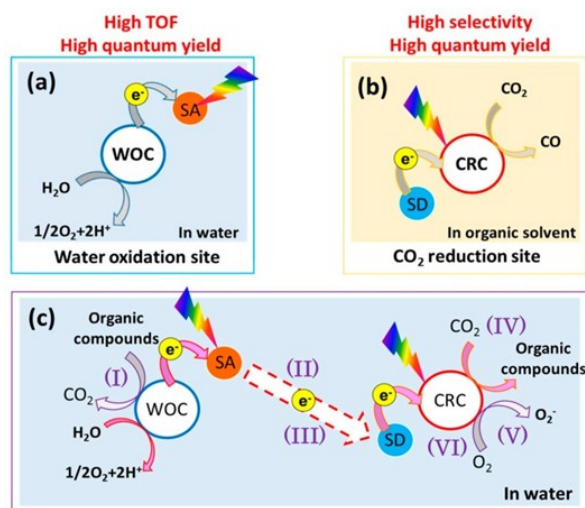
Figure 7. Advantages and disadvantages of metal complex catalysts for CO$_2$ reduction with H$_2$O oxidation (adapted from [8]). (a**) The advantages of H$_2$O oxidation of a metal complex catalyst (H$_2$O oxidation site) with a sacrificial electron acceptor (SA); (**b**) the advantages of CO$_2$ reduction for a metal complex catalyst (CO$_2$ reduction site) with a sacrificial electron donor (SD); (**c**) the problems encountered when combining H$_2$O oxidation site and CO$_2$ reduction site.**

Table **2** shows the summarized data of the catalyst material which used in electrochemical CO$_2$ reduction.

Table 2. Summary of CO$_2$ reduction electrocatalysts from recent literature.

Electrocatalyst	Electrolyte	Selectivity and activity	Stability	Reference
Cu NCs with 44 nm edge length	0.1 M KHCO$_3$	J_{tot} = ≈5.7 mA cm^{-2}, F.E. CO$_2$RR 80%, ethylene 41%, methane 20% @ −1.1 V vs RHE	–	42
Cu mesopore electrode (width/depth)	0.1 M KHCO$_3$	J_{tot} = 14.3 mA cm^{-2}, F.E. C$_2$H$_4$ 38% (30 nm/40 cm) C$_2$H$_6$ 46%(30 nm/70 nm) @ −1.7 V vs NHE; onset potential −0.96 V vs NHE	–	43
3D porous hollow fiber Cu electrode	0.3 M KHCO$_3$	J_{tot} = ≈10 mA cm^{-2}, F.E. CO 75% @ −0.4 V vs RHE	24 h @ −0.4 V vs RHE	44
Cu NPs 13.1 nm	0.1 M KHCO$_3$	J_{tot} = 20 mA cm^{-2}, H$_2$ 0.078, CO 0.016, CH$_4$ 0.0018, C$_2$H$_4$ 0.0006 (Vol. % cm^{-2}) @ −1.1 V vs RHE	–	45
Cu NPs	0.1 M NaHCO$_3$	J_{tot} = ≈9 mA cm^{-2}, F.E. CH$_4$ 80%, H$_2$ 13% @ −1.25 V vs RHE	1 h @ −1.25 V vs RHE	46
OD Cu films	0.5 M NaHCO$_3$	J_{tot} = 2.7 mA cm^{-2}, F.E. CO ≈40%, HCO$_2$H 33% @ −0.5 V vs RHE	7 h @ −0.5 V vs RHE	47
Plasma-activated Cu	0.1 M KHCO$_3$	F.E. C$_2$H$_4$ 60% @ −0.9 V vs RHE; onset E: −0.5 V vs RHE	–	48
OD Au NPs	0.5 M NaHCO$_3$	J_{tot} = 6 mA cm^{-2}, F.E. CO 98% @ −0.4 V vs RHE	8 h @ −0.4 V vs RHE	49
Au$_{25}$ cluster	0.1 M KHCO$_3$	J_{tot} = ≈14.3 mA cm^{-2}, F.E. CO 99.6% @ −0.89 V vs RHE	–	50

The majority of existing CO_2 reduction electrocatalysts can be divided into three groups: metallic, non-metallic, and molecular catalysts. Based on the primary CO_2 reduction product, monometallic catalysts can be further divided into several subgroups: CO selective metals (*e.g.*, Au, Ag, and Zn), formate selective metals (*e.g.*, Sn, In, and Pb), and hydrogen selective metals (*e.g.*, Fe, Ni, and Pt), as shown in Figure 8. Among all the monometallic catalysts, Cu exhibits a distinct catalytic ability to produce a wide range of CO_2 reduction products, including CO, formate, ethanol, and ethylene [51].
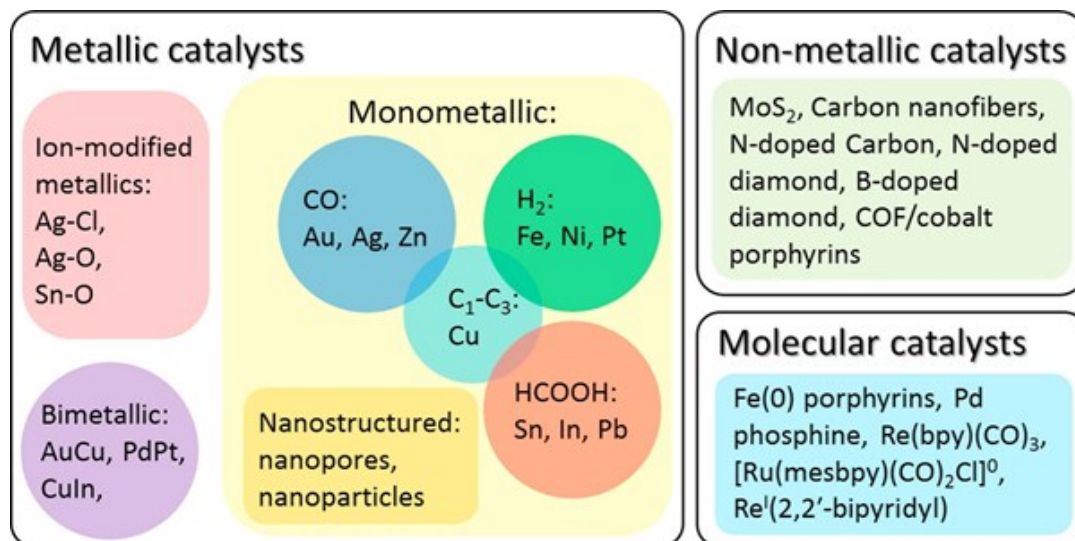

Figure 8. An outline of three major categories of electrocatalysts for CO_2 reduction [51].

4. Result and discussion

In this part, we review the result and discussion of the photocatalytic and electrochemical CO_2 reduction. First, the adsorption and activation of CO_2 on a catalyst surface is the initial step. The activation of adsorbed CO_2 molecules is a crucial and very challenging step for CO_2 reduction. CO_2 adsorption and activation significantly affect subsequent reduction steps and suppression of the competing hydrogen evolution reaction (HER). The adsorption interaction with surface atoms is believed to result in a partially charged species CO_2^{δ}. The possible adsorbed structures of CO_2 mainly include oxygen coordination, carbon coordination, and mixed coordination (in Figure 9). For oxygen coordination, each of the oxygen atoms in CO_2 can donate lone pairs of electrons to surface Lewis acid centers (in Figure 9a). For carbon coordination, the carbon atom in CO_2 could also behave as a Lewis acid and acquire electrons from Lewis base sites, resulting in a carbonate-like structure (in Figure 9b). In contrast, for mixed coordination, both oxygen atoms and carbon atoms in CO_2 act as an electron donor and acceptor at the same time, as shown in Figure 9c [52].
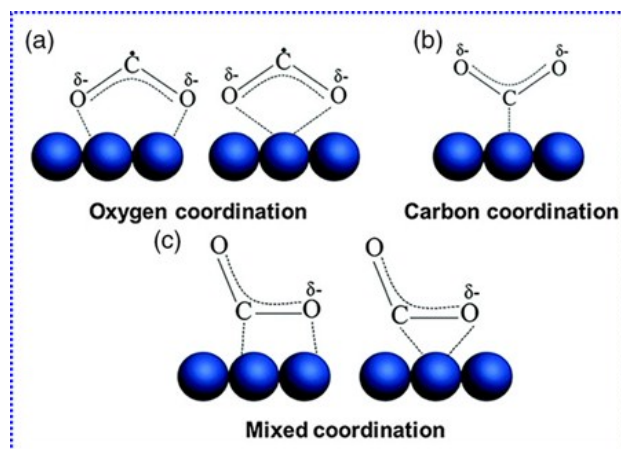
Figure 9. a–c) Three adsorbed CO$_2^\delta$ structures [52].

4.1. *Electrochemical CO$_2$ reduction to Methanol (CH$_3$OH) on electrocatalyst*

Several electrocatalyst materials nominated in CO$_2$ reduction process. The metal alloys, inorganic, and organic–metal compounds, as well as the pyridine-based electrocatalysts have gained a lot of interests attributed to their remarkable selectivity. Recently, metal-free compounds were rapidly developed as they can avoid metal utilization and improve catalytic activity, as well as the high selectivity of MOF electrocatalysts. The recent development on CO$_2$ ECR to CH$_3$OH and discussed in the following sections with different types of electrocatalysts. In addition, NHE, RHE, and SHE are representing normal hydrogen electrode, reversible hydrogen electrode, and standard hydrogen electrode, respectively. The crystal structure, morphology and experiment conditions of various electrocatalysts were summarized.
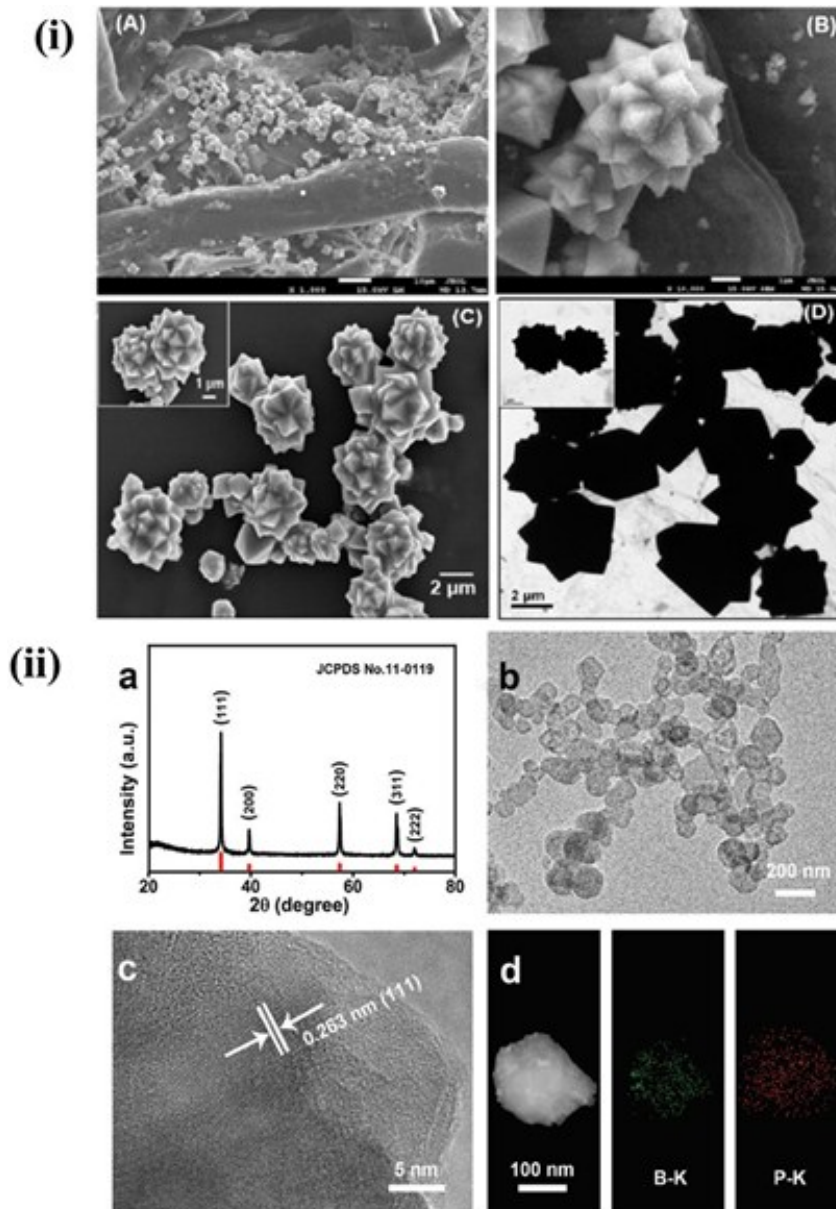
Figure 10. (i) SEM image of Cu₂O(OL-MH)/PPy particles modified LT paper prepared using 6.82 M NaOH, 9.09 mM Cu(NO₃)₂, and 6.26 mM catechin (final concentrations) at 80 °C for 1 h (A). (B) Magnified view of icosahedra (Microflowers) and octahedra structures of Cu₂O. (C) SEM image of Cu₂O(OL-MH)/PPy particles separated from LT paper through sonication. Magnified view of two icosahedra (Microflowers) is displayed in the inset of Fig. 1C. (D) TEM image of Cu₂O(OL-MH)/PPy particles. Inset: magnified view of two icosahedra. (ii) a) XRD pattern of BP. b) TEM and (c) HRTEM images of BP. d) STEM image and corresponding EDX elemental mapping images for BP [53, 54].

Figure 10 express the morphology state, crystal structure and element mapping analysis of the samples. The preparation of the Cu₂O(OL-MH)/PPy particles on the LT

paper occurs through following steps. During immersion of the pyrrole coated LT paper in an alkaline growth solution, pyrrole forms complexes with Cu^{2+} ions that induce the oxidative polymerization of pyrrole to form PPy and Cu+. The Cu+ further forms Cu$_2$O particles in the presence of alkali, oxygen, and catechin as shown in Figure **10i**. The Cu$_2$O particles as seeds then grew to form Cu$_2$O(OL) and Cu$_2$O(OL-MH) on the PPy coated LT paper. Catechin played several important roles in the preparation of Cu$_2$O structures; reducing the Cu^{2+}/pyrrole complexes, stabilizing the particles on the paper surface, controlling the morphology of the particles, and avoiding the formation of CuO. The SEM image displayed in Figure 10i A shows an LT paper possessing icosahedron- and octahedron-like structures of Cu$_2$O(OL-MH)/PPy particles with average diameters of 4.3 ± 0.9 nm and 4.6 ± 0.8 nm, respectively. It is evident from Figure 10i B that Cu$_2$O(OL-MH)/PPy particles are anchored on the surface of LT paper. Figure 10i C shows that Cu$_2$O(OL-MH)/PPy particles separated from the LT paper retained octahedron and icosahedron (micro flower like) morphologies without exhibiting any sonication induced damage. Figure 10i D displays the representative TEM image of Cu$_2$O(OLMH)/PPy particles. The magnified view of two Cu$_2$O(OL-MH)/PPy depicted in the insets of Figure 10i C, D reveals that the particles are decorated with pyramid-like crystal facets. The mapping results for the elements Cu-K, Cu-L, N-K and O-K in the marked areas (1) and (2) further support the elemental composition of both micro flowers and petals, respectively. The X-ray diffraction (XRD) pattern of BP nanoparticles (**Figure 10ii** a) shows four characteristic diffraction peaks at 34.2°, 39.7°, 57.4°, and 68.5° indexed to (111), (200), (220), and (311) planes of cubic BP phase (JCPDS No. 11-0119), respectively. Transmission electron microscopy (TEM) image of BP (Figure 10ii b) indicates the formation of nanoparticles with diameters of 100–200 nm. High-resolution TEM (HRTEM) image (Figure 10ii c) shows the lattice fringes with an interplanar distance of 0.263 nm indexed to the (111) plane of cubic BP. Figure 10ii d shows the scanning TEM (STEM) image of one BP nanoparticle and the corresponding energy-dispersive X-ray (EDX) elemental mapping images, revealing the uniformly distributed B and P elements throughout the BP nanoparticle. The EDX spectrum of BP nanoparticles further reveals the existence of B and P elements and the atomic ratio of B:P is about 1:1.09.

Figure 11i A shows cyclic voltammograms (CVs) of bare, pyrrole coated LT paper, Cu$_2$O(OL)/PPy LT paper and Cu$_{2O}$(OL-MH)/PPy LT paper in CO$_2$ saturated 0.5 M KHCO$_3$ solution. Bare LT paper exhibited a featureless CV, mainly because of its poor conductivity. The LT paper modified with pyrrole did not provide any defined characteristic peak for CO$_2$ reduction. Interestingly, the Cu$_2$O(OL-MH)/PPy LT paper provided higher conductivity and catalytic activity for the reduction of CO$_2$ than the bare, Cu$_2$O(OL)/PPy and pyrrole-coated LT papers. The onset of reduction of CO$_2$ at the Cu$_2$O(OL-MH)/PPy LT paper was determined to be *ca.* -0.43 V vs. RHE, which is 90, 110 and 40 mV lower than that of bare, pyrrole and Cu$_2$O(OL)/PPy-papers, respectively. The Cu$_2$O(OL-MH)/PPy coated LT paper provided a current density of 0.223 mA cm^{-2} at -0.85 V, which is significantly higher than those (0.025, 0.015 and 0.133 mA cm^{-2}) provided by the bare, pyrrole coated and Cu$_2$O(OL)/PPy particles LT papers, respectively.
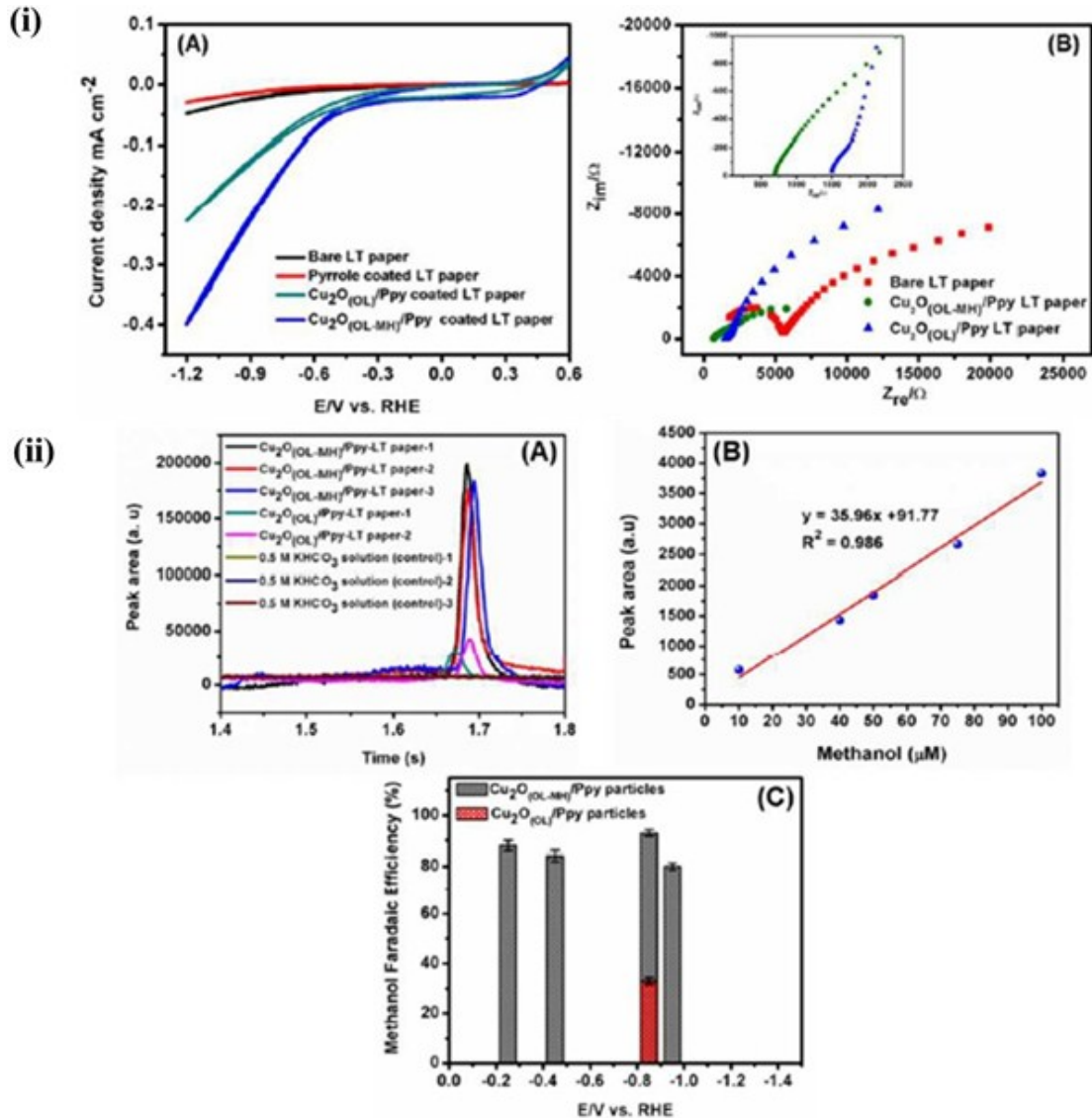
Figure 11. (i) (A) CVs of bare LT paper, pyrrole coated LT paper, $Cu_2O(OL)/PPy$ LT paper, and $Cu_2O(OL-MH)/PPy$ LT paper in CO_2 saturated 0.5 M $KHCO_3$ solution (pH 7.6). Scan rate: 20 mV s-1. **(B)** EIS spectra of the paper electrodes recorded at an amplitude of 5 mV in the frequency range 0.1 Hz to 100 kHz in 0.1 M KCl containing 5 mM $K_3[Fe(CN)_6]$ solution. Inset: magnified view of the EIS spectra. **(ii) (A)** Gas chromatograms (triplicate runs) obtained before and after electrolysis at -0.85 V for 60 min using the $Cu_2O(OL-MH)/PPy$ and $Cu_2O(OL)/PPy$ particles modified LT paper electrodes in CO_2 saturated 0.5 M $KHCO_3$ solution (pH 7.6). **(B)** The calibration plot of methanol and **(C)** the Faradaic efficiency of methanol produced at different potentials. The error bars correspond to triplicate/or duplicate GC runs [53, 54].

Electrochemical impedance spectroscopy (EIS) study was performed to evaluate the conductivity and charge transfer of the paper electrodes. The Nyquist plots of bare LT

paper, Cu$_2$O(OL)/PPy LT paper and Cu$_2$O(OL-MH)/PPy LT paper are displayed in Figure 11i. Bare LT paper exhibits a semicircle with a highest electron transfer resistance (Ret) value of 3549 Ữ, showing its poor conductivity. On the other hand, the Cu$_2$O(OL)/ PPy LT paper and Cu$_2$O(OLMH)/PPy LT paper exhibited straight lines in the low frequency region, corresponding to the Warburg impedance for a diffusion limited process (inset of Figure 11i B). The Cu$_2$O(OL-MH)/PPy LT paper has a defined Warburg curve than that of the Cu$_2$O(OL)/PPy LT paper, indicating improved charge transfer, efficient mass transfer and greater access for the redox species (Fe(CN)$_6$$^{4-/3-}$). Controlled potential electrolysis at the Cu$_2$O(OL-MH)/PPy LT paper electrode was conducted by applying different potentials at -0.25, -0.45, -0.85 or -0.95 V for 1 h in CO$_2$ saturated 0.5 M KHCO$_3$ solution to determine the CO$_2$ reduction products. CO$_2$ saturated electrolyte (0.5 M KHCO$_3$) itself did not provide any signals in the GC spectrum as shown in Figure 11ii A. On the other hand, a sharp peak at a retention time of 1.69 min detected after electrolysis at -0.85 V supports the formation of methanol (Figure 11ii A). It is worthy to note that the methanol peak generated using the Cu$_2$O(OL-MH)/PPy LT paper is several folds higher than that using the Cu$_2$O/PPy octahedra LT paper. From the triplicate GC runs displayed in Figure 11ii A and from the calibration plot displayed in Figure 11ii B, moles of methanol generated at -0.25, -0.45, -0.85 and -0.95 V were calculated, allowing determination of Faradaic efficiencies of methanol to be 88 ± 2.1, 84 ± 2.1, 93 ± 1.2 and 80 ± 1.4%, respectively. Note that the Cu$_2$O(OL-MH)/PPy LT paper provided the highest Faradaic efficiency of 93 ± 1.2% at -0.85V, which is three folds higher than that (33 ± 1.4 %) of the Cu$_2$O(OL)/PPy LT paper (Figure 11ii C). Compared to most reported CO$_2$ reduction catalysts, the Faradaic efficiency (93 ± 1.2%) of methanol determined at the Cu$_2$O(OL-MH)/PPy particles is higher. In conclude, Cu$_2$O(OL-MH)/PPy particles with high index (311) and (211) facets stabilized with the PPy coating exhibited 93% selectivity to single C$_1$ liquid product, methanol. A total of 12 h cycles with the intervals of 2 h in CO$_2$ and Ar-saturated electrolytes at -0.6 V. As shown in **Figure 12i** a, CH$_3$OH is only detected in the CO$_2$-saturated electrolyte. All of the above results conclude that the detected CH$_3$OH is originated from the electrocatalytic CO$_2$RR process over BP/CP. Durability is another important parameter to evaluate catalyst performance. As shown in Figure 12i b, chrono-amperometry curve of BP/CP shows steady current density at -0.6 V for 18 h. The amount of CH$_3$OH approximately increases linearly within 18 h. Recycling experiments were carried out in CO$_2$-saturated 0.1 m KHCO$_3$ solution. As shown in Figure 12i c, BP/CP shows no obvious fluctuation in CH$_3$OH yields and FEs during six recycling tests. All the above results indicate the high electrochemical and structure stability of BP/CP for CO$_2$RR. Note that BP/CP is also capable of converting CO$_2$ into CH$_3$OH with high activity over the wide range of pH (Figure 12i d).
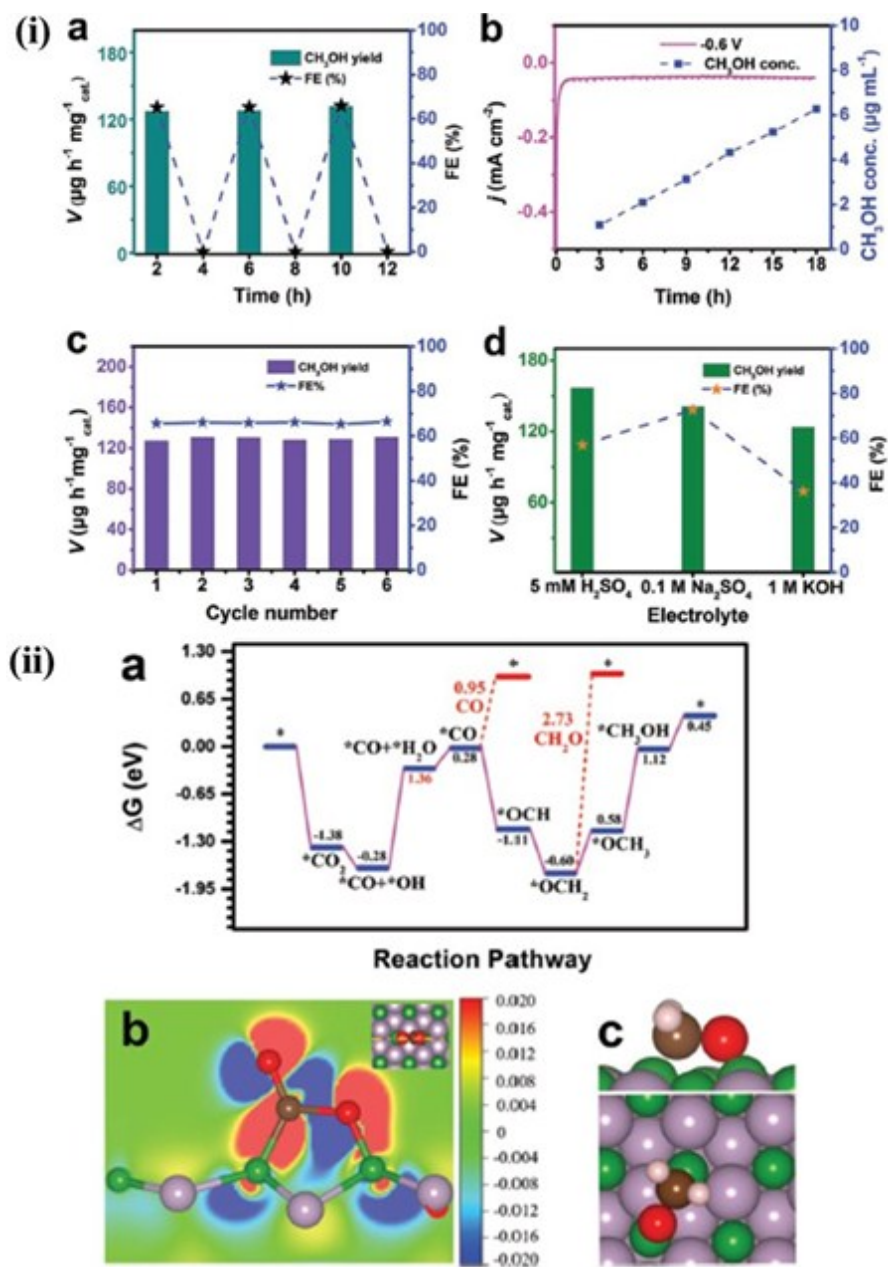
Figure 12. (i) a) CH$_3$OH yields and corresponding FEs for BP/CP with the intervals of 2 h cycles in CO$_2$- and Ar-saturated electrolytes. b) The total current density (left axis) and CH$_3$OH production (right axis) of BP/CP at -0.6 V for 18 h in CO$_2$-saturated 0.1 m KHCO$_3$. c) CH$_3$OH yields and FEs at -0.6 V for recycling tests in 0.1 m KHCO$_3$. d) CH$_3$OH yields at -0.6 V in different electrolytes. (ii) (a) Free energy diagram of CO$_2$RR on BP (111) surface. b) Electron + density difference after CO$_2$ adsorption on BP (111) surface (red and blue colors represent electron accumulation and depletion, respectively). Iso-surface level is 0.02 e Bohr^{-3}. c) Atom configurations of *OCH$_2$ intermediate. B, green; P, gray; C, brown; O, red; H, white [53, 54].

To gain further insight into the catalytic mechanism involved, based on the XRD and HRTEM data, the most exposed BP (111) surface was chosen for DFT calculations. The calculation results show that CO_2 molecule is strongly adsorbed at outermost B sites with DG = -1.38 eV, as shown in **Figure 12ii** a. It suggests that BP (111) surface can effectively adsorb CO_2 molecule, which is crucial in triggering the CO_2RR process. Electron density difference indicates that after CO_2 adsorption, P in BP donates electrons to B, which synergistically activates CO_2 (Figure 12ii b). Bader analysis shows that 1.29 e⁻ are significantly transferred into CO_2 molecule from BP (111), demonstrating CO_2 molecule is effectively activated. The hydrogenated pathway of CO_2 to CH_3OH is calculated in free energy (Figure 4a). Results show that *CO_2 to *CO + *OH process has DG = 0.28 eV, and the process of *CO + *OH to *CO + *H_2O is the most difficult step with DG = 1.36 eV. The subsequent desorption of *H_2O only has a small barrier with DG = 0.28 eV. After H_2O desorption, *CO intermediate desorption is difficult with DG = 0.95 eV, and hydrogenation of *CO to *OCH is a more preferable pathway with DG = 1.11 eV, as shown in Figure 12ii a. The process of *OCH to *OCH_2 is also a downhill pathway with DG = 0.60 eV. It is noteworthy that *OCH_2 intermediate is adsorbed on BP (111) surface by side on coordination with desorption energy of 2.73 eV (Figure 12ii c).

Based on the above theoretical and experimental insights, we propose the formation mechanisms of CO and methanol on the Cu_2O(OL-MH)/PPy particles surfaces (facets). All plausible active sites, intermediates, reaction pathways, and anion exchange processes accounted for the formation of CO and methanol on the Cu_2O(OLMH)/PPy particles surface are identified as schematized in Figure 13A. The dominant (111) facets, high-index (311) and (211) facets, lattice oxygen and oxygen vacancies in Cu_2O promoted efficient adsorption and conversion of CO_2 to form CO_2. CO_2 radical anion species. Wu et al. reported that CO_2 molecules are found to be adsorbed on the oxygen vacancies and high-index facets of Cu_2O that efficiently catalyzed the CO_2 reduction. They noted that changes in the oxygen vacancies at negative potentials generate OH- ions which induce local pH changes close to the surface layer with active sites. The participation of oxygen vacancies in CO_2 reduction has also been explained by Kroger–Vink notation. High-index (311) facets have greater kinks and steps than the low-index (111) facets, which provide improved electrode/electrolyte contact and high surface energies. Because of the improved electrode/electrolyte contact with the high-index (311) crystal facets in Cu_2O(OL-MH)/PPy, the energy barriers for diffusion and mass transport are low, leading to a selective reduction of CO_2 to form methanol as shown in Figure 13B. As revealed from the XPS results, pyrrolic nitrogen atoms in PPy played a dominant role as active sites. The high adsorption capacity of Cu_2O(OL-MH)/PPy particles toward CO_2 resulted from increases in the CO_2 local concentration due to the ability of pyrrolic nitrogen atom of PPy to efficiently adsorb and concentrate CO_2 on the electrode surface from the bulk solution.
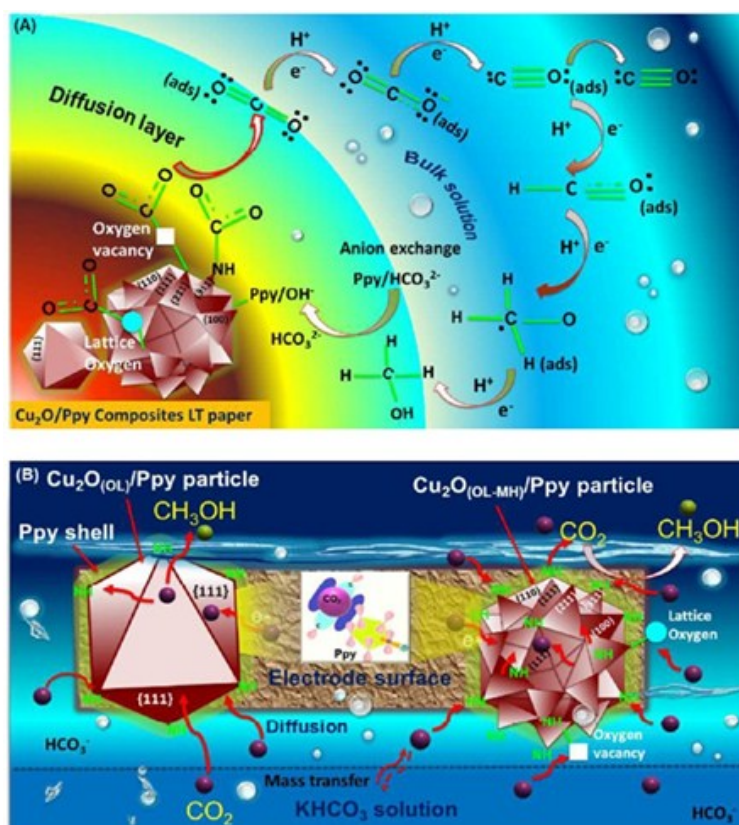
Figure 13. (A) Mechanisms of formation of methanol and CO on the Cu$_2$O(OL-MH)/PPy surface, leading to high durability. (B) Schematic representation of diffusion and mass transport processes at the Cu$_2$O(OL-MH)/PPy particle coated LT paper in CO$_2$ saturated KHCO$_3$ solution [53, 54].

CO$_2$ molecules having two lone pairs of electrons with ("-type bindings formed weak bonds with the ("-electrons in the PPy shell. Since PPy had high CO$_2$ permeability, high CO$_2$ transport, selectivity, and porosity, CO$_2$ molecules readily diffused through the thin PPy shell and adsorbed on the facets of Cu$_2$O. Because of differences between the CO$_2$ molecules being adsorbed on the Cu$_2$O surface and that in bulk solution, a concentration gradient gradually builds near the interface, facilitating the diffusion of CO$_2$ molecules toward the surface. In addition, the PPy shell played several key roles in the observed CO$_2$ molecules having two lone pairs of electrons with ("-type bindings formed weak bonds with the (-electrons in the PPy shell. Since PPy had high CO$_2$ permeability, high CO$_2$ transport, selectivity, and porosity, CO$_2$ molecules readily diffused through the thin PPy shell and adsorbed on the facets of Cu$_2$O. Because of differences between the CO$_2$ molecules being adsorbed on the Cu$_2$O surface and that in bulk solution, a concentration gradient gradually builds near the interface, facilitating the diffusion of CO$_2$ molecules toward the surface. In addition, the PPy shell played several key roles in the observed facets of Cu$_2$O. The relationship between the CO$_2$ reduction activity and shape as well as the exposed low-index and high-index crystal facets of Cu$_2$O was investigated by using various spectroscopic, microscopic and electrochemical techniques.

The Cu_2O(OLMH)/PPy particles modified LT paper provided structure and facet-dependent catalytic activity toward the reduction of CO_2 at ambient conditions, with durability and high flexibility. PPy coating increased the stability, conductivity, and catalytic activity of Cu_2O structures on LT papers. Fuels such as CO and H_2 (syngas), and useful products such as methanol were produced from the reduction of CO_2 with high selectivity. The pyrrolic nitrogen in PPy played a dominant role as active sites for CO_2. It efficiently adsorbed and concentrated CO_2 on the electrode surface from the bulk solution, which increased the CO_2 local concentration, adsorption capacity, and selectivity. In addition, dominant (111) facets favored hydrogen addition to the oxygen atom in H_3CO^- adsorbate instead of a carbon atom, which resulted in high methanol selectivity.

4.2. Photocatalytic CO₂ reduction to Methanol (CH₃OH) on catalyst.

Methanol evolution required 6e⁻ and 6H⁺ which is not easy chemical process compare with CO evolution. A typical process of photocatalytic CO_2 reduction on a semiconductor photocatalyst. It consists of five sequential steps = light absorption, charge separation, CO_2 adsorption, surface redox reaction, and product desorption. The first step is the absorption of photons to generate electron and hole pairs. Illumination of a photocatalyst with the incident light excites electrons from the valance band (VB) to the conduction band (CB), leaving an equal number of holes in VB. In order for these photogenerated electrons or holes to be energetically favorable to reduce CO_2 or oxidize water, photocatalysts should possess suitable band structure. Their CB edge must be more negative than the redox potential of CO_2 reduction, and the VB edge should be more positive than the redox potential of water oxidation (0.817 V vs SHE in pH 7.0 aqueous solution). In addition, photocatalysis has the following two important performance metrics that are frequently cited in literature: *Apparent quantum efficiency (AQE) or external quantum efficiency (EQE)*: AQE or EQE is defined as the number ratio of electrons transferred toward a certain product relative to incident photons at a given wavelength [55]. They can be expressed as the product of the efficiencies of light absorption, charge separation, and surface redox reaction. SFE is defined as the ratio of converted chemical energy relative to the incident solar energy. It can also be understood as the integral of AQE or EQE over the entire solar spectrum. The surface redox reaction is crucial to the whole photocatalytic process. The determination of surface reaction rate is based on reaction product types and reaction mechanisms. There are a great variety of CO_2 reduction products including methanol (CH_3OH) [56], carbon monoxide (CO) [57], methane (CH_4) [58], and so forth. Among all products, CH_3OH is called the new fuel of the 21st century on account of its high energy density and high security and is used as raw material in chemical production widely [59]. Subsequently, CH_3OH is chosen as the reaction product. The reaction routine of CO_2 to CH_3OH is complicated, and there have been several reaction pathways proposed so far including the formaldehyde pathway, the carbene pathway, and the glyoxal pathway [60-63].

Single atom-based photocatalyst, RuSA–mC_3N_4 derived from mC_3N_4 was synthesized as depicted in **Figure 14i**. Briefly, ruthenium salt ($RuCl_{3*-7}H_2O$), dicyanamide, P123 (PEG-

PPGPEG, Pluronic P-123) and tetraethyl orthosilicate (Si source) were utilized as a photocatalyst precursor, the monomer and the template, respectively [64]. In the initial (Figure 14i, stage 1), the dicyanamide is well mixed with calcined SBA-15 for full absorption to facilitate the entry of dicyanamide inside every pore of SBA-15 template and further calcined and treated with HF to remove silica template to get the complete version of mesoporous carbon nitride (mC$_3$N$_4$) (Figure 14i, Stages 2 and 3). Afterward, the harvested mesoporous carbon nitride is employed as photoactive support for the dispersion of ruthenium single atoms (Figure 14i, Stage 4). Aqueous solution of ruthenium (III) chloride was added dropwise under sonication (30 min) to mesoporous carbon nitride followed by microwave (MW) heating (LG, Power 1000 Watt; P/No MEZ66853207) 10–20 times run (2 min each) in Millipore water solution (Figure 14i). By following the described protocol, a single atom RuSA–mC$_3$N$_4$ photocatalyst was synthesized and the authenticity of single atom formation was confirmed via dark-field scanning transmission electron microscopy (HAADF-STEM), and X-ray absorption spectra.
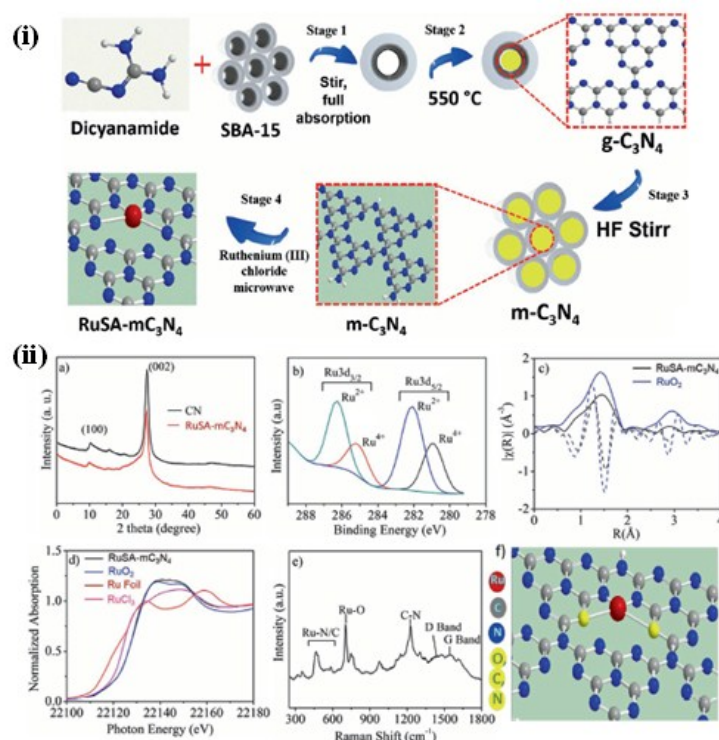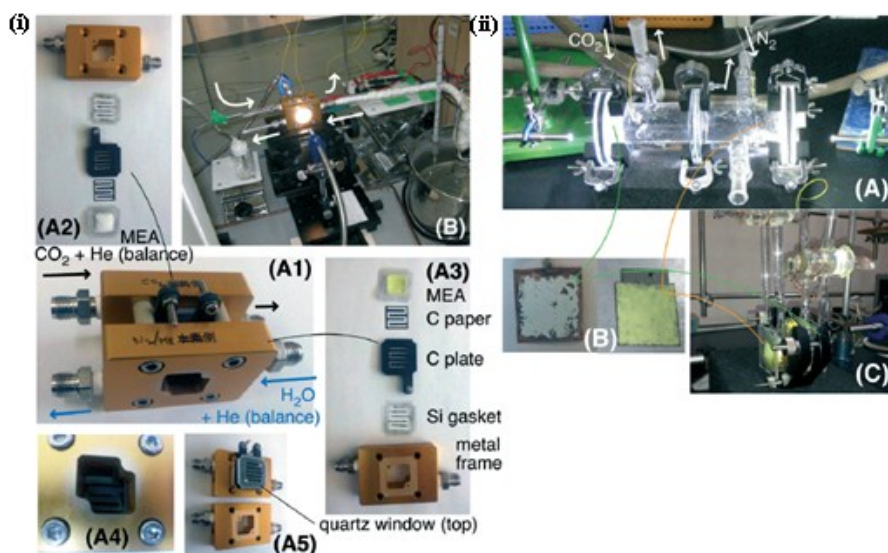

Figure 14. (i) Schematic representation of the synthesis protocol for ruthenium single atom over mesoporous C$_3$N$_4$. RuSA–mC$_3$N$_4$: Ruthenium single atom; mC$_3$N$_4$: mesoporous carbon nitride; SBA-15: Template, HF : Hydrofluoric acid. (ii) a) Wide-angle XRD pattern. b) Ru 3d high-resolution XPS spectra of RuSA–mC$_3$N$_4$. c) Ru K edge Fourier transformation magnitude (solid lines) and imaginary part (dashed lines) EXAFS of RuSA–mC$_3$N$_4$ (black) and RuO$_2$ standard (blue), solid line: magnitude FT, dotted line: imaginary part FT. d) Ru K edge XANES of RuSA–mC$_3$N$_4$ (black), RuO$_2$ standard (blue), RuCl$_3$ standard (pink) and Ru foil (red). e) Raman spectra of RuSA–mC$_3$N$_4$. f) Schematic illustration of the Ru coordination with nitrogen in the CN matrix of RuSA–mC$_3$N$_4$ photocatalyst (N, C, or O based on the Raman spectra) [64, 65].

To ascertain the structural properties, wide-angle XRD measurements were conducted. Wide-angle XRD of the g-C$_3$N$_4$ shows a strong reflection at 27.4° attributed to the interlayer distance of the carbon nitride sheets resembling the 002 reflection of graphite (**Figure 14ii a**). The chemical and elemental composition of catalysts was examined by XPS analysis. In the survey XPS spectrum, peaks at 530, 398, 288, and 287 eV corresponding to O, C, Ru, and N, respectively. The observed XPS results clearly support the absence of metallic ruthenium. Along with ruthenium, the N1s signal band of all the RuSA–mC$_3$N$_4$ was deconvoluted into three nitrogen configurations, including pyridinic-N, pyrrolic-N, and graphitic-N respectively. The main N 1s peak at 398.9 eV is attributed to the sp^2-hybridized pyridinic-N bound to carbon atoms (C-N-C). In addition, the peak at 400.2 eV is related to tertiary N atoms of graphitic-N bonded to C atoms in the form of N-(C)$_3$ and the peak at 401.4 eV can be assigned to the nitrogen linked to hydrogen atoms known as pyrrolic-N referred to C-N-H respectively. The structural changes in the CN scaffold after the Ru doping were also identified from the Raman analysis (Figure 14ii e). The presence of bands in the range of 400–600 and 600–700 cm^{-1} corresponds to Ru–N/C and Ru–O vibration respectively, which further confirms the presence of ruthenium bonded to two different sites. Other bands in Raman spectrum are characteristic C–N, D bands, and G bands of graphic nitrides. However, the broad nature of bands (D and G) suggests a defective structure of the carbon matrix (Figure 14ii e).

Figure 15. (i) Fabricated photo fuel cell-1. The figures show the different components (A) and a photocatalytic test with flowing moisture + He (balance) (front side) and circulating CO$_2$ + He (balance) (rear side) (B). A1 depicts photo fuel cell-1 at the center of B. A2 and A3 depict components of the photocathode and photoanode, respectively. A4 is a view of the window of photo fuel cell-1. A5 depicts the assembled quartz window, silicon gasket, C electrode plate, C paper, silicon gasket, and WO$_3$–Nafion–LDH1 assembly. (ii) Fabricated photo fuel cell-2. The figures show the different components (A) and LDH1 mounted onto Cu foil and WO$_3$ mounted onto water-repellent C paper (B, left to right). The smaller cell-2 was also used in which the LDH1 side (right) was circulated with CO$_2$ gas (C) [65].

CO$_2$ conversion tests using photofuel cell-1 = The fabricated photofuel cell-1 was further tested for its CO$_2$ conversion efficiency. As the first step, all solvents included in the Nafion dispersion solution were removed by flowing N$_2$ gas at a rate of 100 mL min^{-1} through a water bubbler maintained at 343 K, independently to WO$_3$ and LDH1 for 10 h. Subsequently, WO$_3$ in the system was purged with He gas at a rate of 50 mL min^{-1} through the water bubbler at 323 K. CO$_2$ (3.5%) with the remaining He gas (total 101 kPa) was circulated in a glass line at a rate of 450 mL min^{-1} through LDH1 (Figure 15i).

Design of photofuel cell-2 = another designed photofuel cell-2, as shown in Figure 15ii. Photofuel cells were compared for their performance. For the fabrication of photofuel cell-2, 95 mg of WO$_3$ was suspended in 5% of Nafion dispersion solution (0.24 mL) and 1-propanol (0.16 mL) and mounted onto water-repellent C paper in an area of 4 cm^2. WO$_3$ mounted onto the C paper was then covered with a Kapton film (200H, Dupont) of thickness 50 nm and pressed using a tabletop press (SA-302) by applying a pressure of 2.0 MPa at 393 K for 10 min. Then, the Kapton film was carefully removed to obtain the WO$_3$/C photoelectrode (Figure 15ii B, right).

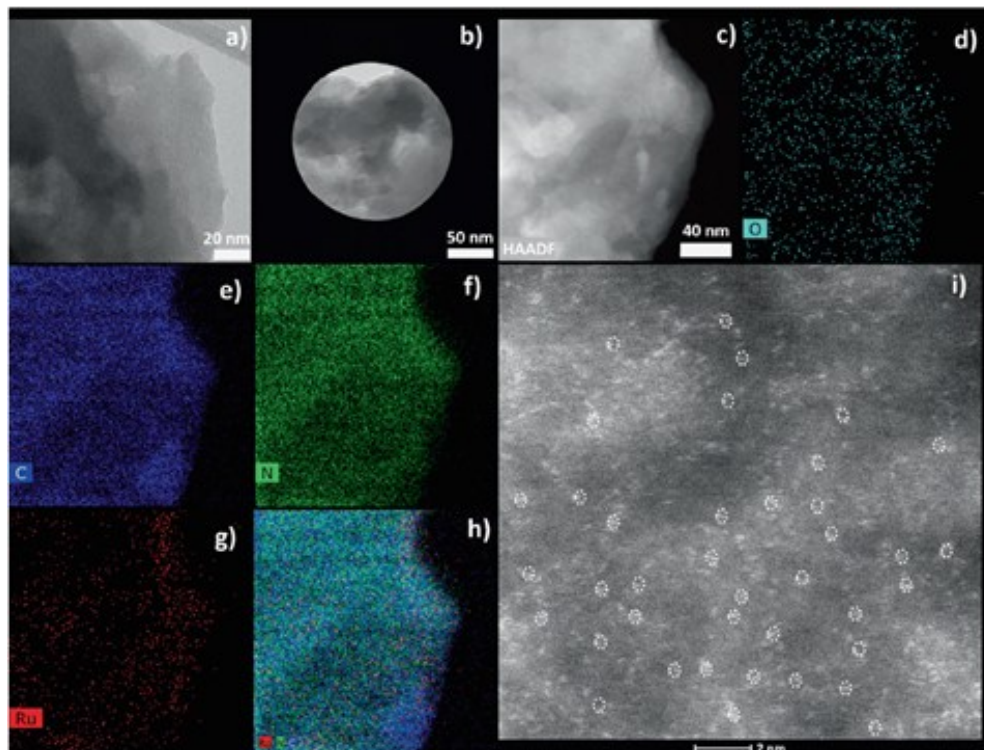**Figure 16. a) TEM image at 20 nm. b) TEM image at 50 nm. c) HAADF image TEM. and d–h) STEM elemental mapping images showing O, C, N, Ru individually and Ru, N, C together (40 nm) and i) STEM image at 2 nm displaying the ruthenium single atom formation over mC$_3$N$_4$ [64].**

Table 3. Comparison of photocurrents generated during the CO$_2$ conversion tests using the photo fuel cells designed in this study.

| Entry	Cell type	WO$_3$^{a} support	LDH1^b support	Current (μA)	e$^-$ flow rate (μmol h^{-1} g$_{LDH}$$^{-1}$)	MeOH or H$_2$ form rate (μmol h^{-1} g$_{LDH}$$^{-1}$)
a	Photofuel cell-1	Nafion film	Nafion film	0.22	0.40^d	0.045 (MeOH)^d
b		Nafion film (C black mixed^e)	Nafion film (C black mixed^e)	0.10	0.18^d	0.029 (MeOH)^d
c	Photofuel cell-2	C paper	Cu foil	1.15	0.96	0.49 (H$_2$)
d		C paper	Cu foil (no Nafion disp sol used^e)	1.63	1.36	0.67 (H$_2$)

^{a} 95 mg. ^{b} 45 mg. ^{c} 0.2 mg. ^{d} Divided by exposed LDH1 sample to light (45 mg × 0.45). ^{e} LDH1 was dispersed in 1-propanol only and mounted on Cu foil.

Table 4. Comparative study of methanol formation performed under varying reaction conditions (Reaction condition: RuSA–mC$_3$N$_4$ (50 mg) photocatalyst, DMF + water (7 mL+1 mL) purged with CO$_2$ for 30 min for saturating the solution with CO$_2$).

S. no.	Catalyst	Condition	Time [h]	Methanol yield [μmol g^{-1}]
1	Blank	Light + CO$_2$$^{a)}$	24	0
2	RuCl$_3$+ mC$_3$N$_4$	Light + CO$_2$$^{a)}$	24	420
3	mC$_3$N$_4$	Light$^{b)}$	24	20
4	RuCl$_3$+gC$_3$N$_4$	Light + CO$_2$$^{a)}$	24	400
5	RuSA–mC$_3$N$_4$	Light$^{b)}$	24	50
6	RuSA–mC$_3$N$_4$	Light + (exposed CO$_2$)$^{c)}$	24	200
7	RuSA–mC$_3$N$_4$	Light + (CO$_2$ purged)$^{d)}$	12	600
8	RuSA–mC$_3$N$_4$	Light + (CO$_2$ purged)$^{d)}$	24	750
9	Nano-RuC$_3$N$_4$	Light + CO$_2$$^{a)}$	24	1000
10	RuSA–gC$_3$N$_4$	Light + CO$_2$$^{a)}$	24	1100
11	RuSA–mC$_3$N$_4$	Light + CO$_2$$^{a)}$	6	1500
12$^{e)}$	RuSA–mC$_3$N$_4$	Light$^{b)}$	24	00

The high-resolution transmission electron microscopy (HRTEM) and TEM images further demonstrate the absence of any ruthenium-based nanoparticles on the surface of mC$_3$N$_4$ sheets (**Figure 16a**). Furthermore, the HAADF-STEM image of RuSA–mC$_3$N$_4$ revealed the individual ruthenium atoms were atomically dispersed, and the corresponding EDS mapping images disclosed the distribution of Ru over the entire mesoporous mC$_3$N$_4$ structure (Figure 16a–i). It seems to have more Ru moieties on the edges that could be due to the presence of comparatively easily accessible uncondensed -NH$_2$ groups of mC$_3$N$_4$. The Ru single atoms are highlighted in white dotted circle in high magnified image (Figure 16i). The presence of all key elements was also confirmed by EDX analysis. Table 3 expressed the comparison of photocurrents generated during the CO$_2$ conversion tests using the photo fuel cells designed in this study. On comparing the photocurrent generated in photofuel cell-1 and photofuel cell-2 with the same types and amounts of photocatalysts, it was observed that photofuel cell-2 generated a higher

photocurrent. This suggests that proton diffusion in the HCl solutions (pH 4) of photofuel cell-2 (Table 1c, d) is sufficiently high and that the diffusion of protons in 50 ìm-thick Nafion film is relatively critical. In addition, Table 4shows the comparative study of methanol formation performed under varying reaction conditions (Reaction condition: RuSA–mC$_3$N$_4$ (50 mg) photocatalyst, DMF + water (7 mL+1 mL) purged with CO$_2$ for 30 min for saturating the solution with CO$_2$).
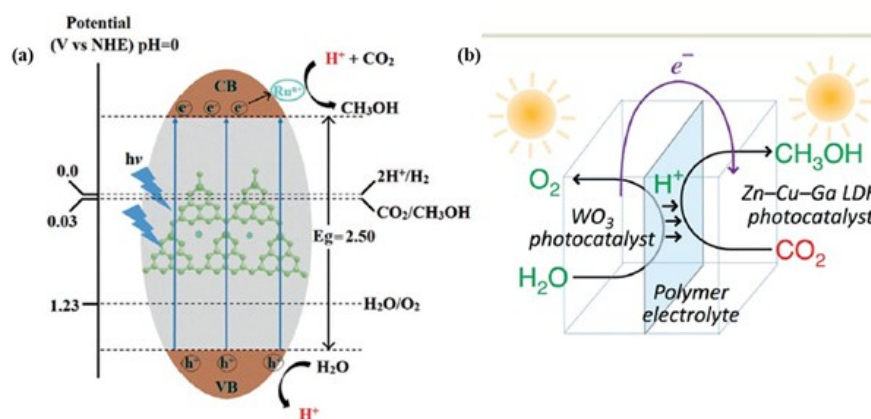
Scheme. (a) Possible schematic representation of photocatalysis mechanism over RuSA–mC$_3$N$_4$ surface under visible light irradiation. (b) Schematic illustration of the flow of materials and electrons during photocatalytic CO$_2$ conversion in reverse photo fuel cell-1 consisting of WO$_3$ and LDH1 [64, 65].

Above scheme illustration shows the possible chemical reaction onto the catalyst surface and the charge transition during the CO$_2$ reduction process. A possible schematic representation of photocatalysis mechanism over RuSA–mC$_3$N$_4$ surface under visible light irradiation is shown in Scheme **a**. In this material, Ru is bounded to sites through Ru-C/N (and or Ru-O) bonds as evidenced by the Raman, EXAFS, and XANES analyses. These sites might be working as a bridge to facilitate the faster electron transfer and enhancing the charge density on Ru thus reducing the photocarrier transfer barrier and enabling the augmented photocatalytic activity of RuSA–mC$_3$N$_4$ for the aqueous reduction of CO$_2$ to methanol (in Scheme a) using water as an electron donor. It is well known that the mechanism underlying the photocatalytic splitting of water using WO$_3$ under UV irradiation is via the following equation. WO$_3$ exhibited constant oxygen generation upon irradiation by UV-visible light in the presence of a sacrificial oxidant (Ag+). The potentials for the photoreduction reactions, e.g., H$_2$ formation, are beyond the bandgap energy of WO$_3$. Thus, the protons generated in this process transferred to LDH1 via Nafion film in the case of photofuel cell-1, and via the acid solution and Nafion film in the case of photofuel cell-2. On the other hand, the electrons generated in this process transferred to LDH1 via the external circuit (Scheme **b**).

5. Conclusion

In conclusion, the photocatalytic performance, crystal structure and charge transfer properties of the photocatalyst are depends on the synthesis method. The synthesis method is divided into 6 ways and each method has specific advantage side. The photocatalyst material highly used for the photocatalytic reduction of CO$_2$. Principle side of photocatalytic CO$_2$ reduction like thermodynamics, mass transfer, and selectivity and reaction mechanism have been deliberated. To further enhance the CO$_2$ reduction performance, improvements can be possibly made from the following two directions. Seeking new material compositions and structures would continue to be at the heart of electrocatalytic and photocatalytic CO$_2$ reduction research. For photocatalytic CO$_2$ reduction, the exploration of new materials and structures can also be greatly accelerated by borrowing knowledge from photocatalytic water splitting. Photocatalytic CO$_2$ reduction and photocatalytic water splitting only differs in their surface reaction step. If strategies (such as incorporation of proper cocatalysts) can be undertaken to significantly shift the cathodic reaction selectivity away from HER to CO$_2$RR, essentially all existing photocatalysts for water splitting can be transformed to those for CO$_2$ reduction. The efficiency of the photocatalytic reaction depends greatly on the efficiency of electron transfer and charge transfer from metal/metal oxide to graphene (carbon material). On the other hand, the photocatalytic carbon dioxide (CO$_2$) reduction in aqueous media provides a potential and convenient way for fulfilling increasing fossil energy demand and relieving global warming problems. In conclusion, the combination of semiconductor with graphene, the charge transfer properties, bandgap, the recombination coefficient and the condition of reduction process are the main factors for the photocatalytic reduction of carbon dioxide. CO$_2$ electrochemical reduction is a process involving transfer of multiple electrons and protons. Because of the low solubility of CO$_2$ in electrolytes, how to deliver CO$_2$ effectively to the cathode surface becomes the key to achieve a high current density and a high CO$_2$ reduction selectivity simultaneously in a practical CO$_2$ electrolyzer.

Reference

1. S. Back, M. S. Yeom, Y. Jung, Active Sites of Au and Ag Nanoparticle Catalysts for CO$_2$ Electroreduction to CO, *ACS Catal.* 2015, **5**, 5089.

2. A. Salehi Khojin, H. R. M. Jhong, B. A. Rosen, W. Zhu, S. Ma, P. J. A. Kenis, R. I. Masel, Nanoparticle Silver Catalysts That Show Enhanced Activity for Carbon Dioxide Electrolysis, *J. Phys. Chem. C* 2013, **117**, 1627.

3. M. Zeng, Y. Li, Recent advances in heterogeneous electrocatalysts for the hydrogen evolution reaction, *J. Mater. Chem. A* 2015, **3**, 14942.

4. M. Asadi, B. Kumar, A. Behranginia, B. A. Rosen, A. Baskin, N. Repnin, D. Pisasale, P. Phillips, W. Zhu, R. Haasch, R. F. Klie, P. Kral, J. Abiade, A. Salehi Khojin, Robust carbon dioxide reduction on molybdenum di-sulphide edges, *Nat. Commun.* 2014, **5**, 4470.

5. G. Xi, S. Ouyang, P. Li, J. Ye, Q. Ma, N. Su, H. Bai, C. Wang, Ultrathin W$_{18}$O$_{49}$ Nanowires with Diameters below 1 nm: Synthesis, Near Infrared Absorption, Photoluminescence, and Photochemical Reduction of Carbon Dioxide, *Angew. Chem., Int. Ed.* 2012, **51**, 2395.

6. T. Wang, X. Meng, G. Liu, K. Chang, P. Li, Q. Kang, L. Liu, M. Li, S. Ouyang, J. Ye, *In situ* synthesis of

ordered mesoporous Co-doped TiO_2 and its enhanced photocatalytic activity and selectivity for the reduction of CO_2, *J. Mater. Chem. A* 2015, **3**, 9491.

7. V. P. Indrakanti, J. D. Kubicki, H. H. Schobert, Photoinduced activation of CO_2 on Ti-based heterogeneous catalysts: Current state, chemical physics-based insights and outlook, *Energy Environ. Sci.* 2009, **2**, 745.

8. Z. Zhang, Y. Huang, K. Liu, L. Guo, Q. Yuan, B. Dong, Multichannel Improved Charge Carrier Dynamics in Well Designed Hetero nanostructural Plasmonic Photocatalysts toward Highly Efficient Solar to Fuels Conversion, *Adv. Mater.* 2015, **27**, 5906.

9. R. Reske, H. Mistry, F. Behafarid, B. Roldan Cuenya, P. Strasser, Particle Size Effects in the Catalytic Electroreduction of CO_2 on Cu Nanoparticles, *J. Am. Chem. Soc.* 2014, **136**, 6978.

10. M.P. Pechini, Method of Preparing Lead and Alkaline-Earth Titanates and Niobates and Coating Method Using the Same to Form a Capacitor-US PAT., **3**.330.697, 1967.

11. X. Chen, S. Shen, L. Guo, S. S. Mao, Semiconductor-based Photocatalytic Hydrogen Generation, *Chem. Rev.* 2010, **110**, 6503.

12. Y. Sohn, W. Huang, F. Taghipour, Recent progress and perspectives in the photocatalytic CO_2 reduction of Ti-oxide-based nanomaterials, *Appl. Surf. Sci.* 2017, **396**, 1696.

13. J. Pan, G. Liu, G. Q. M. Lu, H. M. Cheng, On the True Photo reactivity Order of {001}, {010}, and {101} Facets of Anatase TiO_2 Crystals, *Angew. Chem., Int. Ed.* 2011, **50**, 2133.

14. B. R. Eggins, J. T. Irvine, E. P. Murphy, J. Grimshaw, Formation of two-carbon acids from carbon dioxide by photoreduction on cadmium sulphide, *J. Chem. Soc., Chem. Commun.* 1988, **16**, 1123.

15. B. AlOtaibi, X. Kong, S. Vanka, S. Y. Woo, A. Pofelski, F. Oudjedi, S. Fan, M. G. Kibria, G. A. Botton, W. Ji, H. Guo, Z. Mi, Photochemical Carbon Dioxide Reduction on Mg-Doped Ga(In)N Nanowire Arrays under Visible Light Irradiation, *ACS Energy Lett.* 2016, **1**, 246.

16. Y. Izumi, Recent advances in the photocatalytic conversion of carbon dioxide to fuels with water and/or hydrogen using solar energy and beyond, *Coord. Chem. Rev.* 2013, **257**, 171.

17. X. L. Luo, Z. Yin, M. H. Zeng, M. Kurmoo, The construction, structures, and functions of pillared layer metal–organic frameworks, *Inorg. Chem. Front.* 2016, **3**, 1208.

18. J. Sun, G. Chen, J. Wu, H. Dong, G. Xiong, Bismuth vanadate hollow spheres: Bubble template synthesis and enhanced photocatalytic properties for photodegradation, *Appl. Catal. B: Environ.*, **132** (2013), pp. 304-314.

19. Y. Li, J. Liu, X. Huang, G. Li, Hydrothermal synthesis of Bi_2WO_6 uniform hierarchical microspheres, *Cryst. Growth Des.*, **7** (2007), pp. 1350-1355.

20. R. Buonsanti, V. Grillo, E. Carlino, C. Giannini, T. Kipp, R. Cingolani, P.D. Cozzoli, Nonhydrolytic synthesis of high-quality anisotropically shaped brookite TiO_2 nanocrystals, *J. Am. Chem. Soc.*, **130** (2008), pp. 11223-11233.

21. X.-K. Wang, C. Wang, W.-Q. Jiang, W.-L. Guo, J.-G. Wang, Sonochemical synthesis and characterization of Cl-doped TiO_2 and its application in the photodegradation of phthalate ester under visible light irradiation, *Chem. Eng. J.*, **189** (2012), pp. 288-294.

22. M. Li, C. Bian, G. Yang, X. Qiang, Facile fabrication of water-based and non-fluorinated superhydrophobic sponge for efficient separation of immiscible oil/water mixture and water-in-oil emulsion, *Chem. Eng. J.*, **368** (2019), pp. 350-358.

23. Mao J., Li K., Peng T. Recent advances in the photocatalytic CO_2 reduction over semiconductors. *Catal. Sci. Technol.* **3** (2013), pp. 2481–2498.

24. Yuan L., Xu Y.-J. Photocatalytic conversion of CO_2 into value-added and renewable fuels. *Appl. Surf. Sci.* **342** (2015), pp. 154–167.

25. Takeda H., Koike K., Inoue H., Ishitani O. Development of an efficient photocatalytic system for CO_2 reduction using rhenium (i) complexes based on mechanistic studies. *J. Am. Chem. Soc.* **130** (2008),

pp. 2023–2031.

26. Morris A.J., Meyer G.J., Fujita E. Molecular approaches to the photocatalytic reduction of carbon dioxide for solar fuels. *Acc. Chem. Res.* **42** *(*2009), pp. 1983–1994.

27. Hawecker J., Lehn J.-M., Ziessel R. Efficient photochemical reduction of CO_2 to CO by visible light irradiation of systems containing re (bipy)(CO)₃X or Ru(bipy)₃²⁺–CO²⁺ combinations as homogeneous catalysts. *J. Chem. Soc. Chem. Commun.* (1983), pp. 536–538.

28. Sayama K. *Solar to Chemical Energy Conversion.* Springer; Berlin/Heidelberg, Germany: 2016. Solar hydrogen production on photocatalysis-electrolysis hybrid system using redox mediator and porous oxide photoelectrodes; pp. 345–365.

29. Yang J., Wang D., Han H., Li C. Roles of co-catalysts in photocatalysis and photoelectrocatalytic. *Acc. Chem. Res.* **46** *(*2013), pp. 1900–1909.

30. Hong J., Zhang W., Ren J., Xu R. Photocatalytic reduction of CO_2: A brief review on product analysis and systematic methods. *Anal. Methods.* 5, (2013), pp. 1086–1097.

31. Neau '., Maciá-Agulló J.A., Garcia H. Solar light photocatalytic CO_2 reduction: General considerations and selected bench-mark photocatalysts. *Int. J. Mol. Sci.* 15 (2014), pp. 5246–5262.

32. Hashimoto K., Irie H., Fujishima A. TiO_2 photocatalysis: A historical overview and future prospects. *Jpn. Appl. Phys.* 2005;44:8269.

33. Wang P., Huang B., Dai Y., Whangbo M.-H. Plasmonic photocatalysts: Harvesting visible light with noble metal nanoparticles. *Phys. Chem. Chem. Phys.* 2012;14:9813–9825.

34. Sánchez A., Artola A., Font X., Gea T., Barrena R., Gabriel D., Sánchez-Monedero M.Á., Roig A., Cayuela M.L., Mondini C. CO_2 *Sequestration, Biofuels and Depollution.* Springer; Berlin/Heidelberg, Germany: 2015. Greenhouse gas from organic waste composting: Emissions and measurement; pp. 33–70.

35. Li Y., Wang W.-N., Zhan Z., Woo M.-H., Wu C.-Y., Biswas P. Photocatalytic reduction of CO_2 with H_2O on mesoporous silica supported Cu/TiO_2 catalysts. *Appl. Catal. B Environ.* 2010;100:386–392.

36. Yan S.C., Ouyang S.X., Gao J., Yang M., Feng J.Y., Fan X.X., Wan L.J., Li Z.S., Ye J.H., Zhou Y. A room-temperature reactive-template route to mesoporous $ZnGa_2O_4$ with improved photocatalytic activity in reduction of CO_2. *Angew. Chem.* 2010;122:6544–6548.

37. Liu Q., Zhou Y., Kou J., Chen X., Tian Z., Gao J., Yan S., Zou Z. High-yield synthesis of ultralong and ultrathin Zn_2GeO_4 nanoribbons toward improved photocatalytic reduction of CO_2 into renewable hydrocarbon fuel. *J. Am. Chem. Soc.* 2010;132:14385–14387.

38. Iizuka K., Wato T., Miseki Y., Saito K., Kudo A. Photocatalytic reduction of carbon dioxide over Ag co-catalyst-loaded $ALa_4Ti_4O_{15}$ (A = Ca, Sr, and Ba) using water as a reducing reagent. *J. Am. Chem. Soc.* 2011;133:20863–20868

39. Zhang Q., Li Y., Ackerman E.A., Gajdardziska-Josifovska M., Li H. Visible light responsive iodine-doped TiO_2 for photocatalytic reduction of CO_2 to fuels. *Appl. Catal. A Gen.* 2011;400:195–202.

40. Stock M., Dunn S. $LiNbO_3$—A polar material for solid-gas artificial photosynthesis. *Ferroelectrics.* 2011;419:9–13.

41. Tu W., Zhou Y., Liu Q., Tian Z., Gao J., Chen X., Zhang H., Liu J., Zou Z. Robust hollow spheres consisting of alternating titania nanosheets and graphene nanosheets with high photocatalytic activity for CO_2 conversion into renewable fuels. *Adv. Funct. Mater.* 2012;22:1215–1221.

42. Zhai Q., Xie S., Fan W., Zhang Q., Wang Y., Deng W., Wang Y. Photocatalytic conversion of carbon dioxide with water into methane: Platinum and copper (i) oxide co-catalysts with a core–shell structure. *Angew. Chem.* 2013;125:5888–5891.

43. Giocondi J.L., Rohrer G.S. Spatial separation of photochemical oxidation and reduction reactions on the surface of ferroelectric $BaTiO_3$. *J. Phys. Chem. B.* 2001;105:8275–8277.

44. Kalinin S.V., Bonnell D.A., Alvarez T., Lei X., Hu Z., Ferris J., Zhang Q., Dunn S. Atomic polarization

and local reactivity on ferroelectric surfaces: A new route toward complex nanostructures. *Nano Lett.* 2002;2:589–593.

45.   H.-P. Yang, S. Qin, H. Wang, J.-X. Lu Organically doped palladium: a highly efficient catalyst for electroreduction of CO_2 to methanol, Green Chem, 17 (2015), pp. 5144-5148,

46.   J.H.Q. Lee, S.J.L. Lauw, R.D. Webster The electrochemical reduction of carbon dioxide (CO_2) to methanol in the presence of pyridoxine (vitamin B_6) Electrochem Commun, 64 (2016), pp. 69-73

47.   J.J. Bi, P.F. Hou, F.W. Liu, P. Kang, Electrocatalytic reduction of CO_2 to methanol by iron tetradentate phosphine complex through amidation strategy, ChemSusChem, 12 (2019), pp. 2195-2201

48.
       Y.M. Liu, Y.J. Zhang, K. Cheng, X. Quan, X.F. Fan, Y. Su, S. Chen, H.M. Zhao, Y.B. Zhang, H.T. Yu, M.R. Hoffmann, Selective electrochemical reduction of carbon dioxide to ethanol on a boron- and nitrogen-Co-doped nano diamond, Angew Chem Int Ed, 56 (2017), pp. 15607-15611

49.   Y. Yan, E.L. Zeitler, J. Gu, Y. Hu, A.B. Boca sly, Electrochemistry of aqueous pyridinium: exploration of a key aspect of electrocatalytic reduction of CO_2 to methanol, J Am Chem Soc, 135 (2013), pp. 14020-14023,

50.   Sun S., Wang W., Zhang L., Shang M., Wang L. Ag@C core/shell nanocomposite as a highly efficient plasmonic photocatalyst. *Catal. Commun.* 2009;11:290–293.

51.   P.-Y. Olu, Q. Li, K. Krischer, The true fate of pyridinium in the reportedly pyridinium-catalyzed carbon dioxide electroreduction on platinum, Angew Chem Int Ed, 57 (2018), pp. 14769-14772.

52.   Sun S., Wang W., Zhang L., Shang M., Wang L. Ag@C core/shell nanocomposite as a highly efficient plasmonic photocatalyst. *Catal. Commun.* 2009;11:290–293.

53.   P. Periasamy, R. Ravindranath, S. K. S M, W. Wu, T. Jian and H. Chang, Facet- and Structure-Dependent Catalytic Activity of Cuprous Oxide/Polypyrrole Particles Towards the Efficient Reduction of Carbon Dioxide to Methanol, *Nanoscale*, 2018.

54.   Shiyong Mou , Tongwei Wu , Junfeng Xie , Ya Zhang , Lei Ji , Hong Huang , Ting Wang , Yonglan Luo , Xiaoli Xiong , Bo Tang , Xuping Sun, Boron Phosphide Nanoparticles: A Nonmetal Catalyst for High-Selectivity Electrochemical Reduction of CO_2 to CH_3OH, Adv Mater, 2019 ep;31(36):e1903499.

55.   J. R. Bolton, S. J. Strickler, J. S. Connolly, Limiting and realizable efficiencies of solar photolysis of water, *Nature* 1985, **316**, 495.

56.   S. Feng, X. Chen, Y. Zhou, W. Tu, P. Li, H. Li, *et al.*, $Na_2V_6O_{16}$ xH_2O nanoribbons: large-scale synthesis and visible-light photocatalytic activity of CO_2 into solar fuels, *Nanoscale*, **6** (2014), pp. 1896-1900.

57.   B. Qin, Y. Li, H. Wang, G. Yang, Y. Cao, H. Yu, *et al.*, Efficient electrochemical reduction of CO_2 into CO promoted by sulfur vacancies, *Nano Energy*, **60** (2019), pp. 43-51.

58.   H. Wang, L. Zhang, K. Wang, X. Sun, W. Wang, Enhanced photocatalytic CO_2 reduction to methane over WO_3 $0.33H_2O$ via Mo doping, *Appl Catal B*, **243** (2019), pp. 771-779.

59.   J. Albo, M. Alvarez-Guerra, P. Castaño, A. Irabien, Towards the electrochemical conversion of carbon dioxide into methanol, *Green Chem*, **17** (2015), pp. 2304-2324.

60.   M. Subrahmanyam, S. Kaneco, N. Alonso-Vante, A screening for the photo reduction of carbon dioxide supported on metal oxide catalysts for C1–C3 selectivity, *Appl Catal B*, **23** (1999), pp. 169-174.

61.   N. Sasirekha, S.J.S. Basha, K. Shanthi, Photocatalytic performance of Ru doped anatase mounted on silica for reduction of carbon dioxide, *Appl Catal B*, **62** (2006), pp. 169-180

62.   E. Karamian, S. Sharifnia, On the general mechanism of photocatalytic reduction of CO_2, *Journal of CO_2 Utilization*, **16** (2016), pp. 194-203.

63.   J.-Y. Liu, X.-Q. Gong, A.N. Alexandria, Mechanism of CO_2 photocatalytic reduction to methane and methanol on defected anatase TiO_2 (101): a density functional theory study, *The Journal of Physical Chemistry C*, **123** (2019), pp. 3505-3511.

64.   P. Sharma, S. Kumar, O. Tomanec, M. Petr, J.Z. Chen, Jeffrey T. Miller, Rajender S. Varma, Manoj B.

Gawande, and Radek Zboøil, Carbon Nitride-Based Ruthenium Single Atom Photocatalyst for CO$_2$ Reduction to Methanol, *Small* **17**, (2021), 2006478.

65. M. Morikawa, Y. Ogura, N. Ahmed, S. Kawamura, G. Mikami, S. Okamoto, Y. Izumi, Photocatalytic conversion of carbon dioxide into methanol in reverse fuel cells with tungsten oxide and layered double hydroxide photocatalysts for solar fuel generation, Catal. Sci. Technol., **4**, (2014), 1644.